Journal of Physics: Conference Series

PAPER • OPEN ACCESS

Unified description of low-order above-threshold ionization on and off axis

To cite this article: W Becker and D B Miloševi 2016 *J. Phys.: Conf. Ser.* **691** 012002

View the article online for updates and enhancements.

You may also like

- Dependence of above-threshold ionization spectrum on polarization directions of two-color laser fields
Min Liu, , Ying-Chun Guo et al.
- Electron angular distributions in near-threshold atomic ionization
T Marchenko, H G Muller, K J Schafer et al.
- Above-threshold ionization for very low electron energy
W Becker and D B Miloševi

This content was downloaded from IP address 89.245.22.193 on 05/05/2022 at 09:51

Unified description of low-order above-threshold ionization on and off axis

W Becker[1] and D B Milošević[1,2,3]

[1]Max-Born-Institut, Max-Born-Str. 2a, 12489 Berlin, Germany
[2]Faculty of Science, University of Sarajevo, Zmaja od Bosne 35, 71000 Sarajevo, Bosnia and Hercegovina
[3]Academy of Sciences and Arts of Bosnia and Herzegovina, Bistrik 7, 71000 Sarajevo, Bosnia and Herzegovina

E-mail: wbecker@mbi-berlin.de,milo@bih.net.ba

Abstract. A recently developed unified description of low-order above-threshold ionization (Becker *et al* 2014 *J. Phys. B: At. Mol. Opt. Phys.* **47** 204022; 2015 *J. Phys. B: At. Mol. Opt. Phys.* **48** 151001) is revisited and extended. By considering the rescattering electron energies and angles at the classical cutoffs and the contributions of particular quantum-orbit solutions, it is shown that summing both the backward- and the forward-scattering contributions, within the low-frequency approximation, it is possible to reproduce the observed features of the ATI spectra both for low and high energies and both on and off the laser-polarization axis in the momentum plane.

1. Introduction

Above-threshold ionization (ATI) of rare-gas atoms had been considered a closed chapter of strong-field physics [1, 2, 3, 4] until, with the availability of mid-infrared lasers, unexpected structures in the low-energy velocity map (at energies well below the ponderomotive energy U_p) were observed [5]. These include a series of energy peaks along the polarization axis below $0.1\,U_\mathrm{p}$ called the low-energy structure (LES) [6, 7, 8], another structure at energies below the former referred to as the very-low-energy structure (VLES) [9, 10], a fork-like structure off the polarization axis [11], and a V structure with the 'V' opening on either side of the origin along the axis perpendicular to the laser polarization [12]. All of these structures came unexpected because they are not afforded by a simple tunneling picture. In calculations based on the time-dependent Schrödinger equation, they require the long-range Coulomb potential for their presence.

In our recent papers [13, 14, 15], for a unified description of these low-energy effects we revisited the classical simple-man model and its quantum-mechanical implementation in terms of the improved strong-field approximation (ISFA), the low-frequency approximation (LFA) [16, 17], and the quantum-orbit expansion [1, 18]. It turned out that rescattering into states with low energy, especially forward scattering, generates all of the afore-mentioned effects. We have shown that the angle-dependent energy cutoffs of the various simple-man and quantum orbits are imprinted in the calculated velocity map [11, 13, 14, 15]. The agreement with the various experimental data is good [11]. In particular, the recently observed V structure [12] is very well developed [14]. The afore-mentioned cut-off pattern is independent of the atomic

Content from this work may be used under the terms of the Creative Commons Attribution 3.0 licence. Any further distribution of this work must maintain attribution to the author(s) and the title of the work, journal citation and DOI.
Published under licence by IOP Publishing Ltd

binding potential. However, via the magnitude of its scattering amplitude it determines whether or not the rescattering contributions can successfully compete with the rather structureless contribution of the direct electrons.

In the present contribution, we revisit and extend some aspects of the above-mentioned results, with special emphasis on the rescattering electron energies and angles at the classical cutoffs and the contributions of particular quantum-orbit solutions to the electron spectra in the momentum plane. We show that summing both the backward- and the forward-scattering contributions within the LFA, it is possible to reproduce the observed features of the ATI spectra both for low and high energies and both on and off the polarization axis. We use the length gauge and dipole approximation and employ the atomic system of units ($\hbar = |e| = m = 4\pi\varepsilon_0 = 1$) if not stated otherwise.

2. Differential ionization rate for above-threshold ionization with rescattering

The differential ionization rate for above-threshold ionization with rescattering from a bound state ψ_i, having the ionization energy $E_i = -I_\mathrm{p}$, to a final state of an electron with an asymptotic momentum $\mathbf{p}$, is given by [16, 19, 20]

$$w_{\mathbf{p}i} = 2\pi p \left| T^\mathrm{R}_{\mathbf{p}i} \right|^2, \tag{1}$$

where the rescattering T-matrix element in the saddle-point approximation is proportional to

$$T^\mathrm{R}_{\mathbf{p}i} \propto \sum_s \Delta(t_{0s}, t_s)^{-1/2} \mathcal{M}_{\mathbf{p}\mathbf{k}_\mathrm{s}}(t_s) \langle \mathbf{k}_\mathrm{s} + \mathbf{A}(t_{0s}) | \mathbf{r} \cdot \mathbf{E}(t_{0s}) | \psi_i \rangle \exp[iS(t_{0s}, t_s)]. \tag{2}$$

The sum over s is the sum over the solutions of the system of the two saddle-point equations for the ionization time t_{0s} and the rescattering time t_s, viz.

$$\frac{1}{2}\left[\mathbf{k}_\mathrm{s} + \mathbf{A}(t_0)\right]^2 = E_i, \quad \frac{1}{2}\left[\mathbf{k}_\mathrm{s} + \mathbf{A}(t)\right]^2 = \frac{1}{2}\left[\mathbf{p} + \mathbf{A}(t)\right]^2, \tag{3}$$

where $\mathbf{k}_\mathrm{s} = \int_{t_0}^{t} dt' \mathbf{A}(t')/(t_0 - t)$ is the stationary momentum, $S(t_0, t) = \mathbf{p}^2 t/2 + \mathbf{p}\cdot\boldsymbol{\alpha}(t) + \mathbf{k}_\mathrm{s}^2(t - t_0)/2 - E_i t_0 + \int^{t_0} dt' \mathbf{A}^2(t')/2$ is the action, and the determinant is given by

$$\Delta(t_0, t) = \left[\frac{i(t - t_0)}{2\pi}\right]^3 \left[\left(\frac{\partial^2 S}{\partial t_0 \partial t}\right)^2 - \frac{\partial^2 S}{\partial t_0^2}\frac{\partial^2 S}{\partial t^2}\right]. \tag{4}$$

The electric field is monochromatic with frequency ω and period $T = 2\pi/\omega$ and linearly polarized in the direction determined by the unit vector $\hat{\mathbf{e}} = \hat{\mathbf{x}}$. In this case, the electric field vector is given by $\mathbf{E}(t) = \hat{\mathbf{e}} E_0 \sin\omega t$ and we have $\mathbf{A}(t) = \hat{\mathbf{e}} A_0 \cos\omega t$, with $A_0 = E_0/\omega$, and $\boldsymbol{\alpha}(t) = \hat{\mathbf{e}}(A_0/\omega)\sin\omega t$. The ponderomotive energy is defined by $U_\mathrm{p} = \int_0^T \mathbf{A}^2(\tau) d\tau/(2T) = A_0^2/4$.

The rescattering matrix element can be given in the first Born approximation (FBA) or in the low-frequency approximation (LFA) [16]:

$$\mathcal{M}_{\mathbf{p}\mathbf{k}_\mathrm{s}}(t) = \begin{cases} \langle \mathbf{p} + \mathbf{A}(t) | V_\mathrm{sh} | \mathbf{k}_\mathrm{s} + \mathbf{A}(t) \rangle & \text{(FBA)} \\ \langle \psi^{(-)}_{\mathbf{p}+\mathbf{A}(t)} | \; V \; | \mathbf{k}_\mathrm{s} + \mathbf{A}(t) \rangle & \text{(LFA)} \end{cases}. \tag{5}$$

Here $\psi^{(-)}_{\mathbf{p}}$ is the continuum eigenstate of the Hamiltonian $-\boldsymbol{\nabla}^2/2 + V$ with the atom-specific rescattering potential $V(r)$ modeled by a sum of the Coulomb potential and a short-range potential [16]. The expression in the first Born approximation is simpler since the terms $\mathbf{A}(t)$ cancel. We call this the improved strong-field approximation (ISFA) [20]. In this case, only the

short-range part $V_{\rm sh}$ of the potential V is taken into account since the matrix element for the Coulomb potential is singular for forward scattering, i.e. $\propto (\mathbf{p}-\mathbf{k}_{\rm s})^{-2}$.

According to [13, 18, 19] there are two classes of saddle-point solutions of the system of equations (3): the backward-scattering (BS) solutions, which are classified by the multi-index (α,β,m) in [19], and the forward-scattering (FS) solutions, which are classified by the double-index (ν,μ) in [13]. The names BS and FS are related to the case where the liberated electron has its final momentum $\mathbf{p}$ in the direction of the laser polarization axis $\hat{\mathbf{e}}$. In this case, the solutions to the second equation in (3) are given by $\mathbf{p}+\mathbf{A}(t)=\pm[\mathbf{k}_{\rm s}+\mathbf{A}(t)]$. If the electron immediately after the rescattering at the time t moves in the opposite direction, i.e. if $\mathbf{p}+\mathbf{A}(t)=-[\mathbf{k}_{\rm s}+\mathbf{A}(t)]$, we have backward scattering. FS solutions correspond to the '+' sign in the above equation. They are simpler since for these solutions we have $\mathbf{k}_{\rm s}=\mathbf{p}$ and the second equation in (3) is satisfied for all values of t, while the first equation in (3) can be solved analytically over t_0 [13]. Therefore, for $\mathbf{p}\parallel\hat{\mathbf{e}}$, for a fixed value of $\mathbf{p}$, the solution for t_0 is the same for all values of ν and μ. For other electron emission angles θ ($\cos\theta=\mathbf{p}\cdot\hat{\mathbf{e}}/p$), the system of equations (3) should be solved over t_0 and t. New solutions can be easily obtained starting from the known solutions for $\theta=0$. We keep the name FS for such solutions even for $\theta\neq 0$. On the other hand, the BS solutions $\{t_{0s},t_s\}$ are different for each $s\equiv(\alpha,\beta,m)$. Similarly to the FS solutions, we will call BS solutions the solutions for $\theta\neq 0$ that are obtained starting from the (α,β,m) solution for $\theta=0$.

For the BS solutions we can also use a more precise approximation in which the $\alpha=\pm1$ solutions are combined in the uniform approximation [16, 19]. In this case, the sum over $s\equiv(\alpha,\beta,m)$ in the rescattering T-matrix element is replaced by the sum over (β,m) of the matrix elements which contain the weights and the actions in equation (2) and a linear combination of the Airy function and its first derivative.

3. Rescattering electron energies and angles at the classical cutoff

According to the LFA theory the rescattering ATI rate is determined by the elastic rescattering amplitude (5). This amplitude depends on the electron kinetic energy at the rescattering time $E_s=\left[\mathbf{k}_{\rm s}+\mathbf{A}(t)\right]^2/2=\left[\mathbf{p}+\mathbf{A}(t)\right]^2/2$ and on the scattering angle θ_s at the instant of rescattering. For fixed final electron energy $E_{\mathbf{p}}=\mathbf{p}^2/2$ and final emission angle θ in the laboratory frame the rescattering angle is given by [16]

$$\theta_s=\begin{cases}\varphi & \text{for } k_{{\rm s}x}+A_x(t)\geq 0\\ |\varphi-\pi| & \text{for } k_{{\rm s}x}+A_x(t)<0\end{cases},\quad \tan\varphi=\frac{p\sin\theta}{p\cos\theta+A_x(t)}. \tag{6}$$

Let us analyze, as a function of the final electron emission angle θ, the maximum energy $E_{\mathbf{p}}$, the corresponding energy E_s, and the angle θ_s for various backward (βm) and forward (μ) scattering solutions (for fixed βm (μ) the BS (FS) solutions $\alpha=\pm1$ ($\nu=\pm1$) approach each other for the corresponding maximum energy $E_{\mathbf{p}}$ so that the curves presented in figure 1 do not depend on the values of α (ν)).

For the BS solutions there are two groups of orbits, which are distinguished by the index β. For all angles $0^\circ\leq\theta\leq 90^\circ$, the orbits having $\beta=-1$ have higher final energies $E_{\mathbf{p}}$, higher energies E_s upon return, and larger scattering angles θ_s than those with $\beta=1$. Hence, in all three left-hand plots of Fig. 1 the contributions having $\beta=-1$ are located above those with $\beta=1$. Specifically, for $\theta=0^\circ$ the energy $E_{\mathbf{p}}$ of the $\beta=-1$ solutions monotonically decreases from $10.01\,U_{\rm p}$ for $m=0$ to $8\,U_{\rm p}$ for $m\to\infty$, while for the $\beta=1$ solutions it increases to $8\,U_{\rm p}$ from below. Similarly, for $\beta=-1$ the energies E_s for $\theta=0^\circ$ decrease from $3.17\,U_{\rm p}$ for $m=0$ to $2\,U_{\rm p}$ for $m\to\infty$, while for $\beta=1$ they increase towards the same limit. With increasing angle θ the energies $E_{\mathbf{p}}$ decrease forming a set of almost parallel curves $[E_{\mathbf{p}}(\theta)]_{\beta m}$. For $\theta=90^\circ$, the curves for $\beta=-1$ approach a nonzero value (equal to $1.8\,U_{\rm p}$ for $m=0$ and lower for larger values of m), while the curves for $\beta=1$ all approach the value $E_{\mathbf{p}}=0$. The energy E_s remains

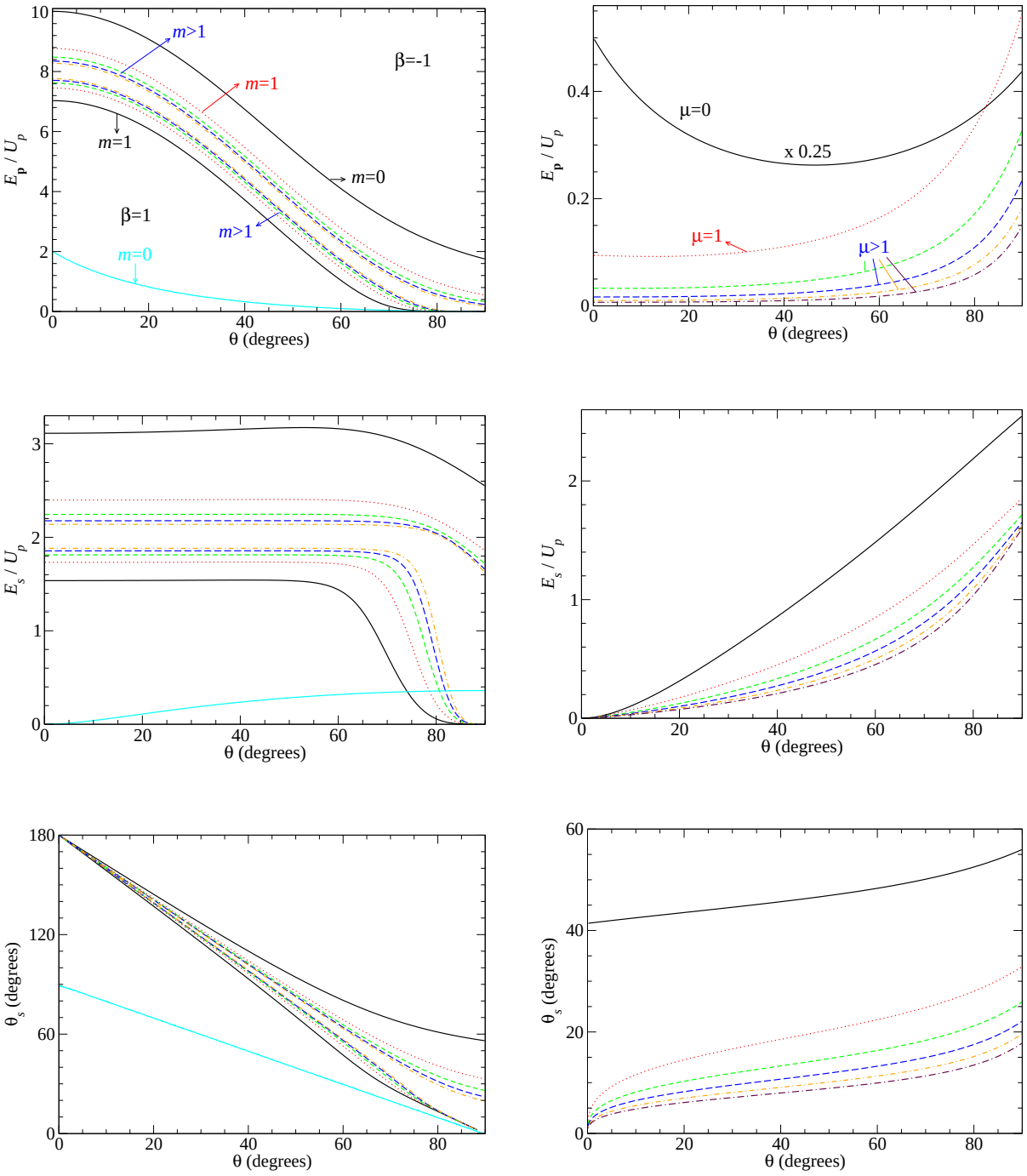

Figure 1. The scattering angle θ_s (lower panels) and the angle-dependent cutoffs of the electron energy E_s at the rescattering time (middle panels) and the final electron energy $E_{\mathbf{p}}$ (upper panels) as functions of the angle θ. The corresponding backward- and forward-scattered quantum-orbit solutions are denoted by the double index (β, m) and the index μ, respectively.

almost constant with increasing θ from zero up to $\approx 60° - 70°$. With a further increase of θ, all energies E_s decrease. For $\beta = -1$ the energies E_s approach nonzero values ($2.55\,U_\mathrm{p}$ for $m = 0$ and lower than $1.87\,U_\mathrm{p}$ for $m \geq 1$), while for $\beta = 1$ all energies quickly decrease to zero. For all solutions, for $\theta = 0°$ the scattering angle θ_s is equal to 180°, which is in accordance with

the fact that the solutions (β, m) are BS solutions (an exception is the recently discovered [18] solution $(\beta, m) = (1, 0)$, presented by a cyan solid line in the left panels of figure 1, which will be commented on at the end of this section). With increasing θ the angle θ_s decreases. For $\beta = -1$ it approaches a nonzero value (for $m = 0$ it is $\theta_s \approx 56^\circ$ for $\theta = 90^\circ$ while for the $m > 0$ solutions we have $\theta_s \approx 20^\circ - 33^\circ$). For $\beta = 1$ the angle θ_s approaches zero for $\theta \to 90^\circ$. Very importantly, according to the Rutherford formula the Coulomb scattering cross section is very large for small values of the angle θ_s and small values of the energy E_s. Now, the orbits characterized by the double index $(\beta, m) = (1, m)$ (which approach the cutoff energy $E_{\mathbf{p}} \approx 8U_\mathrm{p}$ from below for increasing values of m and $\theta = 0^\circ$) have $\theta_s \to 0^\circ$ for $\theta \to 90^\circ$. Hence, they are dominant for emission near right angles to the polarization axis, $\theta \to 90^\circ$. In fact, this explains the experimentally observed outer prongs of the fork-like structures in the off-axis LES [11], as well as the V structure [12, 14].

Let us now analyze the FS orbits. In this case we have only one class of solutions, characterized by the index μ. From the right-hand panels of figure 1 we see that the cutoff energy $E_{\mathbf{p}}$ for the solution $\mu = 0$ (black solid curve; the corresponding energy is multiplied by 0.25) decreases from $2\,U_\mathrm{p}$ at $\theta = 0^\circ$ to $\theta = 46^\circ$ and then increases from $1.05\,U_\mathrm{p}$ to $1.75\,U_\mathrm{p}$ at $\theta = 90^\circ$. The corresponding energy E_s increases from zero for $\theta = 0^\circ$ to a large value above $2.54\,U_\mathrm{p}$ for $\theta = 90^\circ$, while the corresponding angle θ_s increases from $\theta_s = 42^\circ$ to $\theta_s = 56^\circ$. On the other hand, for the solutions with $\mu \geq 1$ both E_s and θ_s go to zero for $\theta \to 0^\circ$, so that the corresponding differential cross sections are very large and these solutions are responsible for the experimentally observed on-axis LES [6, 7, 8]. From the upper right panel of figure 1 one can see that these LESs appear for energies $E_{\mathbf{p}}$ below $0.1\,U_\mathrm{p}$. With increasing angle θ the energies $E_{\mathbf{p}}$ and E_s, as well as the angle θ_s, increase. The angle θ_s remains relatively small even for $\theta = 90^\circ$ (for $\mu = 1, 2, 3, 4, 5, \ldots$ the corresponding values of θ_s are $32.8^\circ, 25.9^\circ, 22.0^\circ, 19.6^\circ, 17.7^\circ, \ldots$). The final electron energy $E_{\mathbf{p}}$ (in units of U_p) for $\theta = 90^\circ$ approaches relatively large values (for $\mu = 1, 2, 3, 4, 5, \ldots$ they are $0.54, 0.33, 0.23, 0.18, 0.15, \ldots$; these values are the same as for the BS solution $\beta = -1$ and $m = \mu$ so that the BS and the FS solutions merge). We note that the FS solutions with $\mu \geq 1$ are responsible for the middle prongs of the off-axis LES observed in [11].

It is surprising that for the BS (FS) solution $\beta m = 10$ ($\mu = 0$) we found that for $\theta = 0^\circ$ the scattering angle θ_s is different from 180° (0°). The reason is that for these solutions classical considerations are inadequate. The classical cutoff for these solutions, $E_{\mathbf{p}} = 2\,U_\mathrm{p}$ [14, 15], corresponds to the travel time $\tau = t - t_0 = 0$, so that $t = t_0$ and $p + A(t) = k + A(t) = k + A(t_0) = 0$. Therefore, for $\theta = 0^\circ$ both the nominator and the denominator of the second equation in (6) are equal to zero, so that we can obtain a nonzero value for θ_s. Quantum-mechanically we have $p + A(t) \neq 0$ so that we obtain $\theta_s = 0^\circ$ for $\mu = 0$ and the corresponding differential cross section is large. This is important because only the solution $\mu = 0$ from the FS solutions contributes in the energy region $\approx U_\mathrm{p}$ and modifies the spectrum of the direct electrons. It should also be mentioned that the solution $\mu = 0$ ($\beta m = 10$) corresponds to the sign "+" ("−") in equation (11) in [15]. For $\theta > 0$, with increasing τ, the classical solution of the saddle-point equations $E_{\mathbf{p},\mu=0}(\tau)$ [15] increases and has a θ-dependent maximum as can be seen in the lower panel of figure 2 in [15]. On the other hand, for $\theta > 0$, with increasing τ, the classical energy $E_{\mathbf{p},\beta m=10}(\tau)$ continuously decreases from a maximum value towards zero (see the upper panel of figure 2 in [15]). With increasing θ, this maximum value decreases from $E_{\mathbf{p}} = 2\,U_\mathrm{p}$ for $\theta = 0^\circ$ to zero for $\theta = 90^\circ$ (see the upper left panel of figure 1).

4. Spectra in the electron momentum plane

In experiments it is common to exhibit the electron spectra in the momentum plane $(p_\perp, p_\parallel) = (p_y, p_x) = (p\sin\theta, p\cos\theta)$. We first present the electron spectra that correspond to the BS quantum orbits. In the left (right) panels of figure 2 we show partial spectra for $\beta = -1$ ($\beta = +1$) and for $m = 0$ ($m = 1$), $m = 1$ ($m = 2$), and $m = 2$ ($m = 3$) in the upper, middle, and

lower panel, respectively. The results presented are in accordance with the results of section 3 and with the classical analysis in figure 3 in [11] and references [14, 15]. For example, the radii of the rescattering rings of the $\beta = -1$ orbits are all larger than those of the $\beta = 1$ orbits, and the former enclose the origin while the latter all intersect exactly at the origin (the uniform approximation that is used cannot be employed close to the origin). As already mentioned, near the $p_\perp$ axis the $\beta = 1$ rings make up the outer prongs of the fork and also build the V structure. Moreover, quantum interferences of the orbits $\alpha = \pm 1$, which are taken into account in the uniform approximation, are clearly visible in each panel.

Next, in figure 3 we present the ISFA spectra obtained using the saddle-point method (equations (1)–(5) for FBA), for particular FS solutions μ. In the lower right panel we present the coherent sum of the contributions of the solutions $\mu = 0, \ldots, 7$, while in the remaining panels we display the partial contributions of the solutions $\mu = 1, 2$ and 3, as denoted. All spectra exhibit a characteristic diamond-like structure and the cutoff values in p_x and p_y decrease with increasing μ. The cutoffs in p_x are located at the LES momenta whose approximate values are $4\sqrt{U_\mathrm{p}}/[(2\mu + 1)\pi]$ [23, 24]. If we were to sum the partial contributions for $\mu = 1, 2, 3, \ldots$ incoherently, we would obtain nested diamonds (rhombi) similar to those of figure 3 in [11]. Instead, for the coherent sum presented in the lower right panel, we now have a characteristic interference pattern inside the largest diamond (the one corresponding to the solution $\mu = 1$). It should be mentioned that if we were to use the LFA instead of the ISFA the spectra would be enhanced for small values of the momenta and the angle θ, which is caused by the Coulomb effect (large differential cross section). The LES for $\mu = 1, 2$ and 3 would then stand out more distinctly.

In figure 4 we present the coherent sum of both BS and FS quantum-orbit contributions. The three prongs of the fork-like structure of the off-axis LES [11] are clearly visible. The differential cross section depends on the rescattering angle at the instant of the recollision. This dependence not only causes the Coulomb-induced enhancements in the low-energy region, it also modifies the high-energy spectra, which are described by the BS solutions. This is clearly visible in figure 4 where we see characteristic minima for particular values of the angle θ. These minima are atom-specific and similar results have already been obtained for short-wavelength lasers [16]. For a fixed value of θ, from the middle left panel of figure 1 we can read off the electron energy E_s at the rescattering time, while from the lower left panel we obtain the corresponding scattering angle θ_s. For example, we see that for $\theta \approx 20^\circ$ we have $E_s \approx 3U_\mathrm{p}$ and $\theta_s \approx 140^\circ$. For these parameters the differential cross section for elastic scattering of an electron off the xenon positive ion exhibits a minimum. The situation can be reversed in the sense that from a measured ATI electron spectrum in the momentum plane one can extract information about the differential positive-ion cross section [21] (this is particularly useful for the molecular case [22]).

5. Conclusions

In this paper we have shown in detail in figure 1 how the cutoffs of the electron energy (both for the returning electron at the rescattering time and for the final energy at the detector) and the rescattering angle at the time of rescattering depend on the lab-frame electron angle (with respect to the laser polarization axis). This was done both for back-scattering (BS) and forward-scattering (FS) quantum orbits, which are classified by the index (β, m) and μ, respectively. From this figure all aspects of the electron spectra can be extracted. Foe example, from the right panels it is evident that for the $\mu = 1, 2, \ldots$ quantum orbits both the electron energy and the rescattering angle are small for the on-axis spectra. The corresponding differential cross section for electron–parent-ion rescattering is then very large due to the Coulomb potential so that the LES clearly appears in the spectra. This is also in agreement with the soft-recollision model [23, 24] (E_s is small).

In figures 2 and 3 we have shown partial spectra for particular BS and FS quantum orbits.

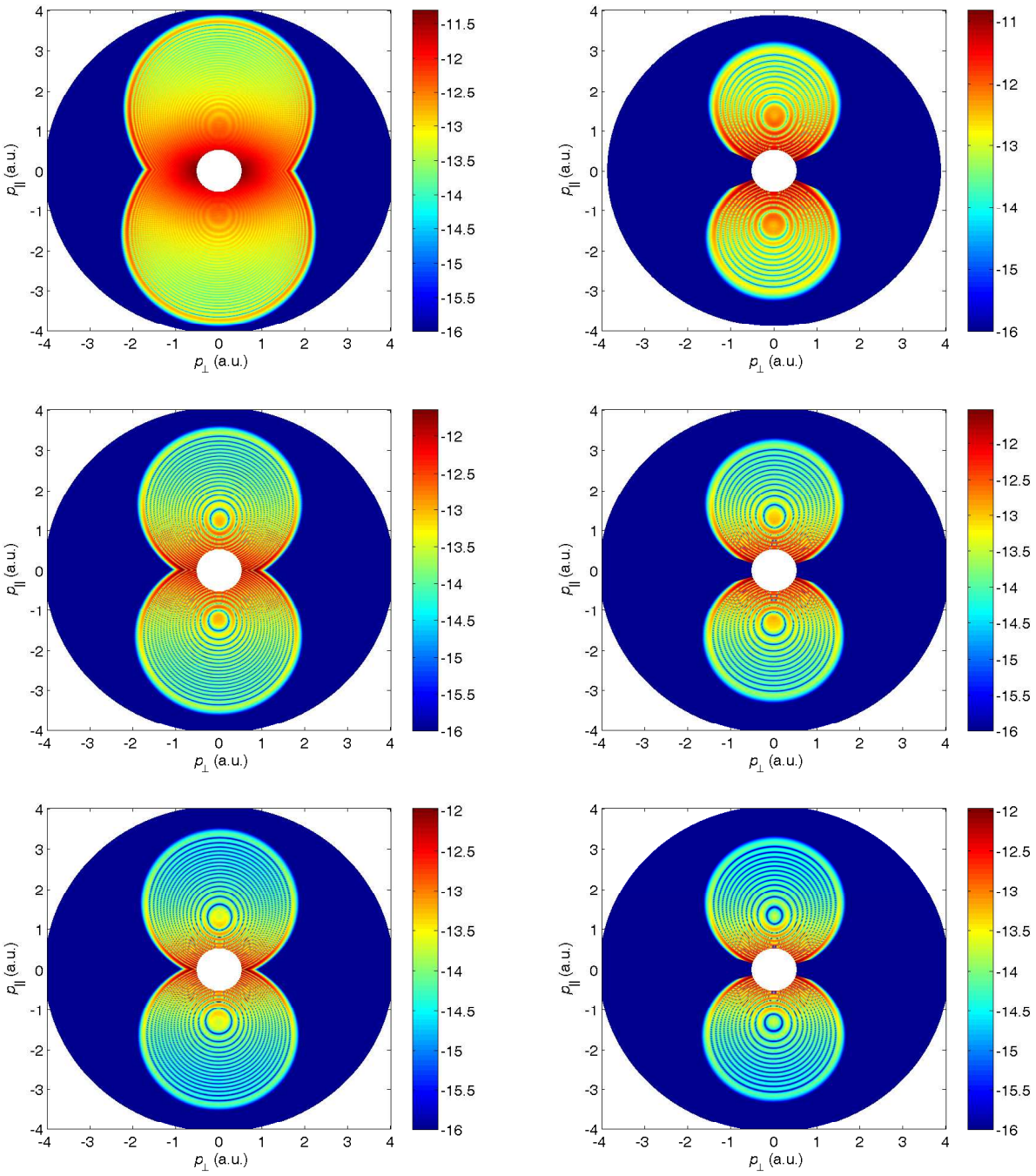

Figure 2. The logarithm of the differential ionization rate of Xe presented in false colors (the color map covers more than four orders of magnitude in arb. units) in the electron momentum plane for ionization by a linearly polarized laser field having the intensity 5×10^{13} W/cm^2 and the wavelength 2000 nm. The results are obtained using the uniform approximation with only one saddle-point solution (β, m). For $\beta = -1$ we present the results for $m = 0$ (upper left panel) $m = 1$ (middle left panel), and $m = 2$ (lower left panel), while for $\beta = +1$ we have $m = 1$ (upper right panel), $m = 2$ (middle right panel), and $m = 3$ (lower right panel).

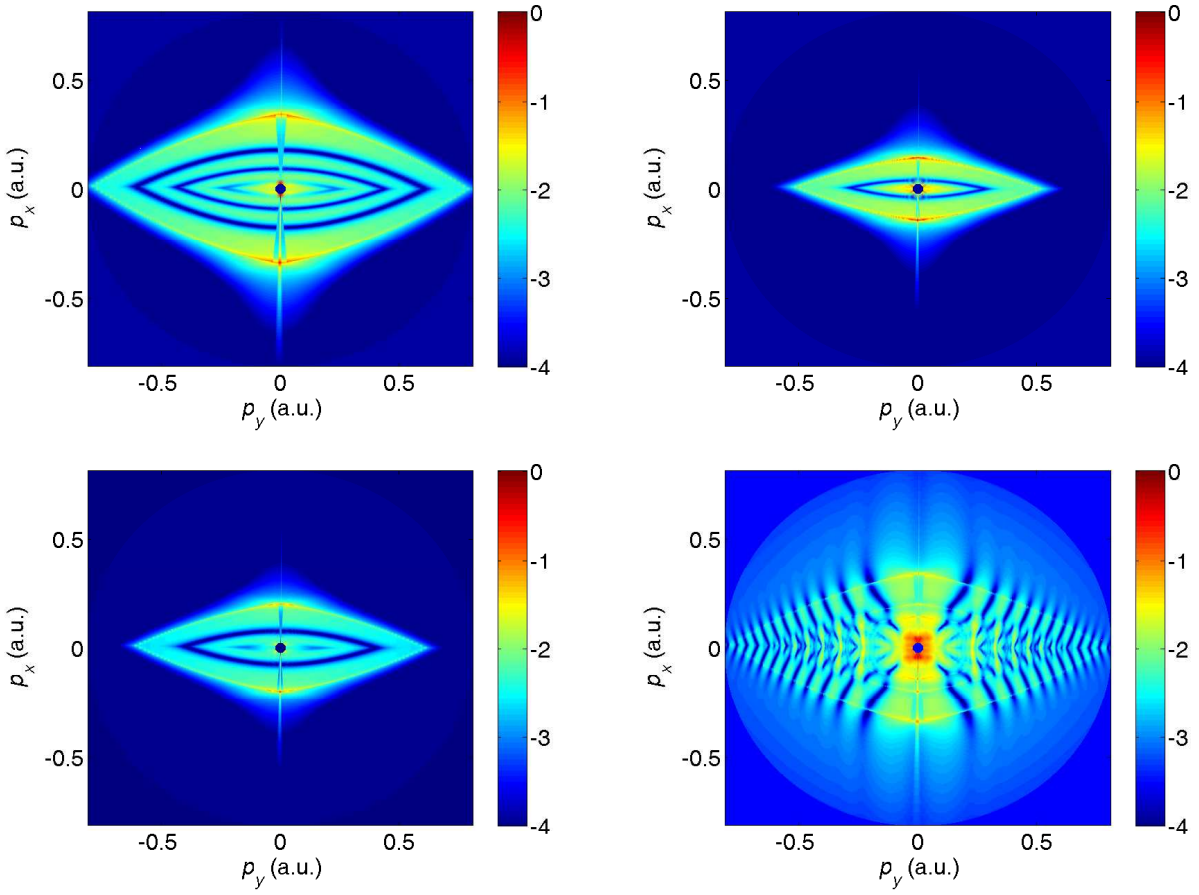

Figure 3. The logarithm of the differential ionization rate of Xe, obtained using the ISFA and the saddle-point method, presented in false colors (the color map covers four orders of magnitude and the rates are normalized to one) in the electron momentum plane for ionization by a linearly polarized laser field having the intensity 4.5×10^{13} W/cm^2 and the wavelength 1800 nm. The results are obtained using the forward-scattering contribution $\mu = 1$ (upper left panel), $\mu = 2$ (lower left panel), $\mu = 3$ (upper right panel) and the coherent sum of the eight solutions $\mu = 0, \ldots, 7$ (lower right panel).

All features of the electron spectra can be explained using these figures. The coherent sum of all quantum-orbit contributions (figure 4) exhibits all the mentioned features. Especially, we retrieved the so-called fork structure, which is located at approximately right angle to and on either side of the polarization axis, both the two outer prongs and the central (split) prong. It should be emphasized that all of these features are already afforded by the ISFA (improved strong-field approximation), which corresponds to the first-order Born approximation for the rescattering electron. The LFA (low-frequency approximation) goes beyond this, essentially by replacing the scattering amplitude in the first-order Born approximation by the exact scattering amplitude (in the absence of the laser field). This way, for higher electron energies the atom-specific minima for particular values of the lab-frame angle also become visible.

References

[1] Becker W, Grasbon F, Kopold R, Milošević D B, Paulus G G and Walther H 2002 Above-threshold ionization: from classical features to quantum effects *Adv. At. Mol. Opt. Phys.* **48** 35

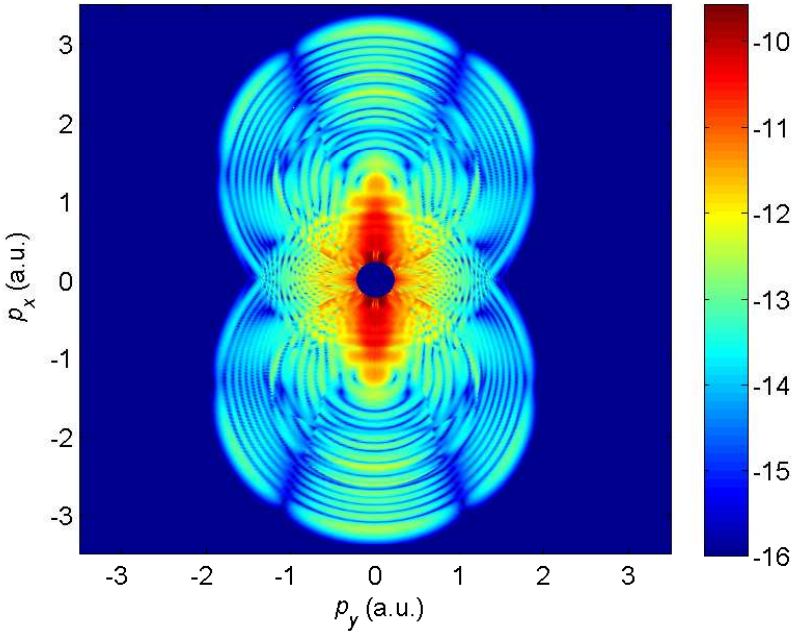

Figure 4. The logarithm of the differential ionization rate of Xe presented in false colors in the electron momentum plane for ionization by a linearly polarized laser field having the intensity 4.5×10^{13} W/cm^2 and the wavelength 1800 nm. The results are obtained as coherent sum of forward-scattering contributions and backward-scattering contributions (taken in the uniform approximation). The rescattering matrix element is calculated in the low-frequency approximation.

[2] Milošević D B, Paulus G G, Bauer D and Becker W 2006 Above-threshold ionization by few-cycle pulses *J. Phys. B: At. Mol. Opt. Phys.* **39** R203
[3] Krausz F and Ivanov M 2009 Attosecond physics *Rev. Mod. Phys.* **81** 163
[4] Agostini P and DiMauro L F 2012 Atomic and molecular ionization dynamics in strong laser fields: from optical to x-rays *Adv. At. Mol. Opt. Phys.* **61** 117
[5] Wolter B, Pullen M G, Baudisch M, Sclafani M, Hemmer M, Senftleben A, Schröter C D, Ullrich J, Moshammer R and Biegert J 2015 Strong-field physics with mid-IR fields *Phys. Rev.* X **5** 021034
[6] Blaga C I, Catoire F, Colosimo P, Paulus G G, Muller H G, Agostini P and DiMauro L F 2009 Strong-field photoionization revisited *Nat. Phys.* **5** 335
[7] Catoire F, Blaga C I, Sistrunk E, Muller H G, Agostini P and DiMauro L F 2009 Mid-infrared strong field ionization angular distributions *Laser Phys.* **19** 1574
[8] Quan W, Lin Z, Wu M, Kang H, Liu H, Liu X, Chen J, Liu L, He X T, Chen S G, Xiong H, Guo L, Xu H, Fu Y, Cheng Y and Zu X X 2009 Classical aspects in above-threshold ionization with a midinfrared strong laser field *Phys. Rev. Lett.* **103** 093001
[9] Wu C Y, Yang Y D, Liu Y Q, Gong Q H, Wu M, Liu X, Hao X L, Li W D, He X T and Chen J 2012 Characteristic spectrum of very-low-energy photoelectrons from above-threshold ionization in the tunneling regime *Phys. Rev. Lett.* **109** 043001
[10] Dura J, Camus N, Thai A, Britz A, Hemmer M, Baudisch M, Senftleben A, Schröter C D, Ullrich J, Moshammer R and Biegert J 2013 Ionization with low-frequency fields in the tunneling regime *Sci. Rep.* **3** 2675
[11] Möller M, Meyer F, Sayler A M, Paulus G G, Kling M F, Schmidt B E, Becker W and Milošević D B 2014 Off-axis low-energy structures in above-threshold ionization *Phys. Rev.* A **90** 023412
[12] Wolter B, Lemell C, Baudisch M, Pullen M G, Tong X-M, Hemmer M, Senftleben A, Schröter C D, Ullrich J, Moshammer R, Biegert J and Burgdörfer J 2014 Formation of very-low-energy states crossing the ionization threshold of argon atoms in strong mid-infrared fields *Phys. Rev.* A **90** 063424

[13] Becker W, Goreslavski S P, Milošević D B and Paulus G G 2014 Low-energy electron rescattering in laser-induced ionization *J. Phys. B: At. Mol. Opt. Phys.* **47** 204022
[14] Becker W and Milošević D B 2015 Above-threshold ionization for very low electron energy *J. Phys. B: At. Mol. Opt. Phys.* **48** 151001
[15] Becker W and Milošević D B 2015 Quantum-orbit theory of low-energy above-threshold ionization on and off axis *Chin. Opt. Lett.* **13** 070006
[16] Čerkić A, Hasović E, Milošević D B and Becker W 2009 High-order above-threshold ionization beyond the first-order Born approximation *Phys. Rev.* A **79** 033413
[17] Milošević D B 2014 Low-frequency approximation for above-threshold ionization by a laser pulse: low-energy forward scattering *Phys. Rev.* A **90** 063423
[18] Milošević D B 2014 Forward- and backward-scattering quantum orbits in above-threshold ionization *Phys. Rev.* A **90** 063414
[19] Milošević D B, Hasović E, Busuladžić M, Gazibegović-Busuladžić A and Becker W 2007 Intensity-dependent enhancements in high-order above-threshold ionization *Phys. Rev.* A **76** 053410
[20] Hasović E, Busuladžić M, Gazibegović-Busuladžić A, Milošević D B and Becker W 2007 Simulation of above-threshold ionization experiments using the strong-field approximation *Laser Phys.* **17** 376
[21] Lin C D, Le A T, Chen Z, Morishita T and Lucchese R 2010 Strong-field rescattering physics–self-imaging of a molecule by its own electrons *J. Phys. B: At. Mol. Opt. Phys.* **43** 122001
[22] Gazibegović-Busuladžić, Hasović E, Busuladžić M, Milošević D B, Kelkensberg F, Siu W K, Vrakking M J J, Lépine F, Sansone G, Nisoli M, Znakovskaya I and Kling M F 2011 Above-threshold ionization of diatomic molecules by few-cycle laser pulses *Phys. Rev.* A **84** 043426
[23] Kästner A, Saalmann U and Rost J M 2012 Electron energy bunching in laser-driven soft recollisions *Phys. Rev. Lett.* **108** 033201
[24] Kästner A, Saalmann U and Rost J M 2012 Energy bunching in soft recollisions revealed with long-wavelength few-cycle pulses *J. Phys. B: At. Mol. Opt. Phys.* **45** 074011